



Ultra-high precision NiP mirror fabrication using ion beam figuring for space applications

PARESH PRADHAN,¹  RILEY SHURVINTON,¹ CYRIL BOURGENOT,²  HONGCHANG WANG,^{1,*} AND KAWAL SAWHNEY¹ 

¹*Diamond Light Source, Harwell Science & Innovation Campus, Didcot OX11 0DE, UK*

²*Durham University, Centre for Advanced Instrumentation, NETPark Research Institute, Joseph Swan Road, Sedgefield TS21 3FB, UK*

**hongchang.wang@diamond.ac.uk*

Abstract: Nickel phosphorous (NiP) is a broadly used optical material for wide-field visible to mid-infrared instrumentation in space applications. The process chain usually involves applying an electroless metal deposition onto a mirror substrate, which is then machined by single-point diamond turning (SPDT). However, the SPDT process leaves low- and mid-spatial frequency errors, which degrades the optical performance. In this work, we demonstrate the use of ion beam figuring (IBF) to correct the low-spatial frequency errors. IBF is a noncontact technique used in the final step of a mirror fabrication, which can precisely correct the surface form errors via a deterministic, stable, and fully computer-controlled process. We report on an IBF process which improves the surface quality of the NiP-coated flat and spherical mirrors. For the flat mirror, the root mean square (RMS) height error over a clear aperture (CA) area of $25 \times 15 \text{ mm}^2$ has been improved from 16.3 nm to 3.4 nm after the IBF process. Similarly, for a spherical mirror, the surface irregularity has been reduced from 13.8 nm to 4.4 nm RMS. These irregularities were eventually limited by the diamond turning marks, which could not be corrected or attenuated with the IBF. For further improvement of the surface quality of the NiP mirror, one flat mirror was polished on a lapping tool (chemical and mechanical polishing) and processed through IBF. The surface quality of the NiP mirror achieved a 1.9 nm RMS surface irregularity over a CA of $20 \times 10 \text{ mm}^2$.

© 2025 Optica Publishing Group under the terms of the [Optica Open Access Publishing Agreement](#)

1. Introduction

Reflective metal optics offer significant advantages over their glass counterparts, such as ease of manufacturing, the ability to produce freeform surfaces [1,2], suitability for additive manufacturing [3], ruggedness, and their capacity to be incorporated into a thermal system [4,5]. They offer good optical performance and structural support of the optical system [6,7], as both the mirror mount and optics can be made of the same material which reduces thermal deformation of the system due to different thermal expansion coefficients of the materials. These properties are noteworthy for applications with lightweight requirements and temperature-variable environments, such as aerospace [8,9]. Therefore, metal-based optical mirrors are increasingly being used in the field of space observation and astronomy.

Aluminium (Al) is one of the most commonly used materials for making mirrors for space applications due to its lightweight, good machinability, thermal conductivity, and low cost [10,11]. It can be easily machined into complex mirror shapes, including spherical, aspherical, and freeform surfaces. Al mirrors can also be additively manufactured or 3D printed to achieve a design that offers specific lightweight or stiffness performance; however, such mirrors usually require a post-processing step, such as CNC machining and single-point diamond turning (SPDT), to achieve the required optical quality [12]. Nevertheless, this quality remains insufficient for applications in the visible spectrum [13]. Therefore, electroless nickel-phosphorus (NiP) is

frequently used to apply a thick and defect-free coating to improve the surface quality of the metal mirrors.

NiP is an amorphous coating with high phosphorus content and can be layered up to a few hundred microns thick [14,15]. NiP-coated metal mirrors have excellent machinability, and the process usually follows another stage of SPDT machining to achieve the final surface shape [16]. While SPDT is highly efficient, low cost, and allows for deterministically creating complex freeform surfaces, it typically introduces a range of spatial frequencies on the surface, which have an increasing impact on the image quality as the wavelength gets shorter. In the IR wavelength range, these spatial frequencies have less impact, and the attenuation of the spatial frequencies through post-polishing is less crucial.

High-spatial frequency (HSF) errors, also called micro-roughness, cause light loss through surface scattering and can also create diffraction and interference effects. SPDT also introduces low-spatial frequency (LSF) to mid-spatial frequency (MSF) errors on the machined surface. LSF errors are usually seen as surface form defects, primarily affecting wavefront quality and reducing imaging performance. MSF errors (also known as waviness), on the other hand, are form errors which (particularly for parts machined through SPDT) generally appear as periodic concentric ripples on the surface, with a pitch between 10 μm and 1 mm reaching heights of up to several ten of nanometres. These errors are produced during the spiral path by various factors, such as vibrations, tool cutting edge waviness and a small variation in the tool position.

In visible (VIS) and ultraviolet (UV) light application, NiP surfaces require an additional post-polishing step to remove these residual errors and achieve a high-quality optical surface. Several traditional polishing methods have been used to improve the surface quality of NiP mirrors, such as float polishing [17], fluid jet polishing (FJP) [18,19], and chemical mechanical polishing (CMP) [20,21]. For example, Namba *et al.* [17] used float polishing method to remove SPDT tool marks and achieve an exceptionally low surface roughness of 0.23 nm RMS. However, float polishing has the disadvantage of low efficiency. Similarly, FJP can eliminate diamond turning marks and improve surface roughness but its ability to improve the LSF and MSF errors is limited. CMP is a surface treatment method that combines chemical corrosion and abrasive removal [22,23]. Recently, Xu *et al.* [21] used CMP with a specific slurry to remove diamond turning marks and achieve a low surface roughness of 0.22 nm RMS on a NiP-coated metal mirror. Although all these traditional polishing methods for NiP coating result in good surface roughness and significant improvement in HSF errors, they are not highly effective in correcting LSF errors. In some cases, traditional polishing tools can deform the final shape of the mirror, generating new LSF errors on the optical surface that need correction for optimal instrument performance.

As an advanced optical manufacturing technology, there are several state-of-the-art techniques available to correct LSF errors on optical surfaces, such as FJP, elastic emission machining (EEM), magnetorheological finishing (MRF), and ion beam technology (IBT) [24]. Anthony *et al.* [19] used FJP to achieve a surface roughness of 1.7 nm RMS followed by bonnet polishing to further improve the surface quality, though this is a complex process. MRF differs significantly from conventional polishing methods; it uses a unique shear removal mechanism that enables material removal at the micron or even nanometre scale, resulting in ultra-smooth surfaces with nanometre precision [25,26]. Recently, Xu *et al.* [27] applied MRF to improve both surface shape errors and surface roughness. Inspection of the NiP-coated mirror after MRF using a laser interferometer showed an improvement in surface shape error from 71.8 nm RMS to 9.6 nm RMS and a reduction in surface roughness from 2.05 nm to 0.70 nm RMS. Ulitschka *et al.* [28] used reactive ion beam etching (RIBE) with nitrogen, followed by oxygen gas, to reduce waviness and surface roughness, achieving a waviness of ~ 10 nm RMS and micro-roughness of 3.5 nm RMS. Similarly, Bauer *et al.* [29] used RIBE with nitrogen gas to improve the paraboloidal surface shape and remove an average of 100 nm material. Despite this, the paraboloidal shape

remained 125 nm from the ideal shape. To address this, ion beam planarization (IBP) was used to remove diamond turning marks and achieve a surface roughness of 0.7 nm RMS. IBP involves an additional photoresist coating, allowing an incident angle at which the NiP can be etched at nearly the same rate as the photoresist [30]. Through several iterations of etching, diamond turning marks can be removed to achieve a low surface roughness. While IBP is promising for enhancing micro-roughness, it is not effective in improving surface form errors. For surface form error correction, ion beam figuring (IBF) can be used.

IBF is a deterministic, non-contact figuring technique, commonly employed for fabricating high-quality, X-ray mirrors for synchrotron radiation and X-ray free electron lasers [31–33]. It removes material using a collimated ion beam through physical sputtering process [34,35]. With its very low removal rate, IBF enables sub-nanometre figure error correction. The ion beam's high stability over time allows precise, controlled material removal, achieving accurate control of the manufactured mirror shape (see Section 3). Consequently, IBF can potentially improve the form errors of optical systems in all types of materials such as NiP [36]. While FJP is quite effective in removing SPDT marks, form correction is best achieved with MRF and IBF. These two techniques offer similar performance in terms of form correction but differ in running costs and hardware requirements. MRF performance is linked to the tool radius and can be more expensive to operate, whereas IBF has no intrinsic limitations regarding mirror geometry and is more cost-effective to run. Therefore, IBF could be applied to strongly curved freeform surfaces with high curvature. Here, we used the IBF technique to improve the surface form error of NiP mirrors.

In this work, NiP-coated mirrors were designed and manufactured to test the capability of IBF for form error correction. The samples themselves cannot be considered for a specific space program. However, these types of ultra precise mirrors could be used in a specific space program [37]. The work is divided into several sections as follows. In Section 2, we discuss the sample fabrication and characterization techniques, along with the IBF system. Section 3 cover the principles and limitations of ion beam figuring. In Section 4, we present the results as follows: first, the surface form error correction of a flat mirror; second, the surface form error correction of a spherical mirror; and third, the surface form error correction after removal of diamond turning marks. Finally, we discuss the effect of the IBF process on the mid- and high-spatial frequency-dependent surface waviness and roughness.

2. Material and methods

2.1. Sample preparation

In this work, an aluminium alloy mirror with a size of 30 mm × 20 mm and thickness of 20 mm has been designed and fabricated in RSA443, a rapidly Solidified alloy made from AlSi40 (Al 60 wt% and Si 40 wt%) and sold by RSP technology (Netherlands). Next, NiP with a high phosphorus content of 6-9% was uniformly deposited onto the AlSi40 substrate using Electroless Nickel Plating (ENP). ENP was conducted in a plating solution where a chemical reaction took place. The high phosphorous content in the coating forms an amorphous structure and reduces the hardness of the coating. It is also important to control the coating's thickness, as an insufficient layer thickness can damage the surface during processing. The NiP coating thickness was approximately 100 µm. After coating, SPDT was performed to machine the sample surface and achieve the required surface shape. SPDT is a three-axis, ultraprecision computer-controlled system. A C-axis is used to rotate the mirror, an X-axis provides linear movement of the diamond tip at a constant in-feed of 3 µm, and a Z-axis linear motion, controlled as a function of C and X axes, creates the depth profile needed for a curved surface [38]. The SPDT was undertaken at Durham University on a Moore Nanotech 250UPL, and the samples were machined with a tool of radius 0.425 mm, a feed rate of 5 mm/min, a spindle speed of 2000RPM and a depth of cut of 2 µm. The sample, mounted on the SPDT machine, is shown in Fig. 1.

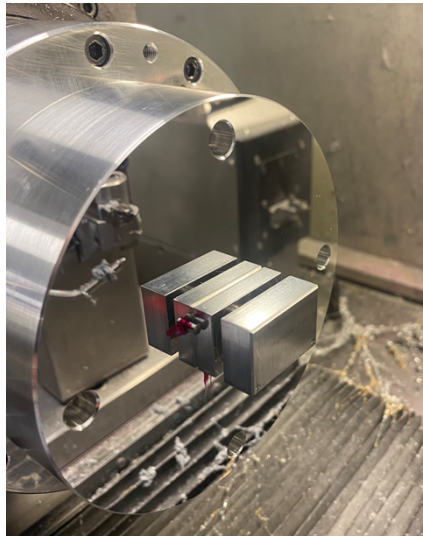


Fig. 1. Sample during SPDT at Durham University.

2.2. Surface metrology

The low-spatial frequency (LSF) errors of the mirrors were measured using an in-house stitching interferometry system at the Optics & Metrology Laboratory in Diamond Light Source. This system includes a four-axis motion stage, enabling roll (θ_x), pitch (θ_y), and horizontal (X) and vertical (Y) translation of the optic, and a Zygo Verifire HDX Fizeau interferometer [39]. The Verifire HDX has a 150 mm (6 inches) diameter field of view, and a stabilized laser beam with both spot and ring mode operation. The interferometer's charge-coupled detector (CCD) has a pixel size of $46 \mu\text{m} \times 46 \mu\text{m}$ and a resolution of 3392×3392 . Data acquisition and processing

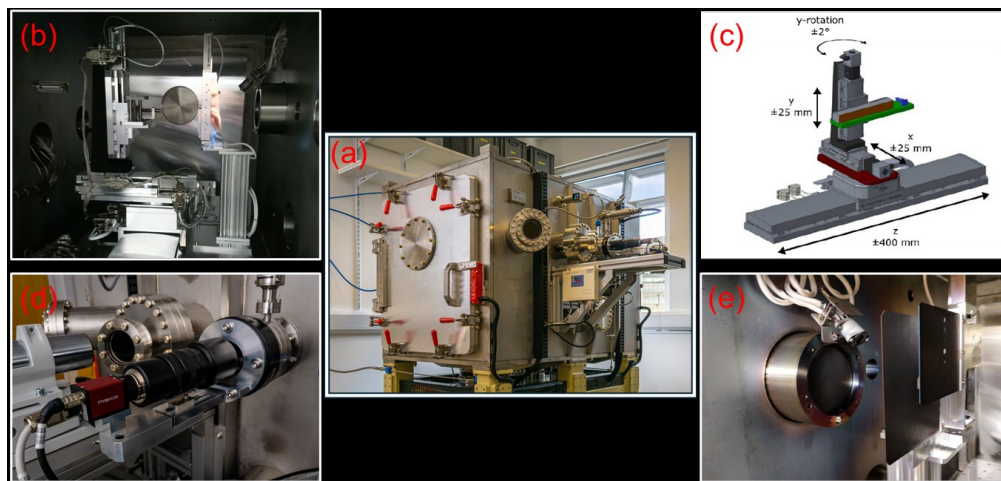


Fig. 2. Photographs of the IBF system and its components: (a) external view of the IBF system, (b) internal view of the IBF system, (c) schematic 3D model showing the motion stages, sample holder, and Faraday cup detector, (d) high-resolution camera for sample alignment, and (e) primary and secondary aperture plate mounts.

were performed using a custom Python code integrated with Zygo Mx software. Before stitching, individual interferograms are pre-processed in Mx using Python scripts. For stitching, multiple overlapping sub-aperture measurements of the surface were carefully combined ('stitched') using Python Large Optics Stitching (PyLOSt) to create a composite image of the entire optical surface.

To characterize the mid- and high-spatial frequency errors, "Contour GT-X" micro-interferometry from Bruker [40] was used. The surface roughness of the AlSi40 sample coated with NiP was investigated using the GT-X in phase shifting interference mode with objectives with magnification of 2.5 \times , 10 \times , and 50 \times . Additionally, it includes two field lenses, 0.55 \times and 2 \times to further adjust the magnification factor of the objectives. The GT-X can produce a 3D micro-topographic map of the surface with a vertical resolution < 0.05 nm RMS over a field of view ranging from 3 mm to 130 μ m and an in-plane resolution of 10 μ m to 0.1 μ m. The system has a motorized sample stage with 300 mm of translation in the X and Y directions, as well as vertical translation for focusing and a tip/tilt adjustment ($\pm 7^\circ$) to orientate the sample. All motion stages are motorized and programmable, including the selection of objectives and field lenses. The instrument can automatically optimize light intensity, tip/tilt, and focus.

2.3. Ion beam figuring system

For this work, the sample surface form error has been corrected using an in-house developed IBF system at Diamond Light Source [41]. Figure 2 presents photographs of the different components of the IBF system. The IBF system is built with a stainless-steel high-vacuum chamber (ultimate pressure $\sim 1 \times 10^{-7}$ mbar) with dimensions of approximately 1.6 m in length, 0.9 m in width, and 1.0 m in height. The system primarily consists of a four-axis motion stage (X, Y, Z, and θ_y), a large diameter DC gridded collimated ion source, and a CCD camera.

In this IBF setup, the ion beam remains stationary while the mirror to be corrected is moved using by the four-axis motion stage. The chamber and motion stages accommodate mirrors up to 300 mm \times 50 mm. A high-resolution camera is used to identify fiducial marks on the sample surface and position the mirror's clear aperture (CA) relative to the ion beam. The ion flux is provided by a stable and constant Argon ion (Ar⁺) beam with a diameter of 120 mm, produced by a KDC100 source and 99.999% pure Ar gas at a fixed flow rate of 7.0 sccm, resulting in a working gas pressure of $\sim 3 \times 10^{-4}$ mbar. The ion beam's shape and size are controlled by two pyrolytic graphite aperture plates. The first graphite plate remains stationary, allowing a central 20 mm \times 10 mm section of the ion beam to pass. A second aperture plate refines the beam shape by passing it through one of several smaller apertures with various shapes (circular or rectangular) and dimensions (1 mm to 10 mm). This secondary aperture plate is mounted on a vertical translation stage, enabling selection of different aperture sizes without compromising the chamber's vacuum. Coarse alignment of the ion beam position is determined using a Faraday Cup (FC 66B, Kimball Physics Inc. USA) detector, and fine adjustments have been done by finding the center coordinates of etched craters on a sample surface.

3. Ion beam figuring principle

IBF is a non-contact, physical sputtering process. In IBF, ions are accelerated to a few hundreds or thousands of electron volts and collide with atoms at the target surface. These atoms gain a certain momentum and energy through a series of cascades, and if an atom's kinetic energy exceeds its binding energy, it is ejected from the surface. This results in material removal at the targeted position. The IBF process is a deterministic technique typically applied at the final stage of the optics manufacturing. Notably, IBF corrects the LSF errors without altering the MSF and HSF errors of the mirror surface as shown in Fig. 3. The process involves a few steps:

First, the optic's surface form error is measured. In this work, we used stitching interferometry to measure the surface height map of the optics, as mentioned in Section 2.2, which we refer to as the HDX surface map.

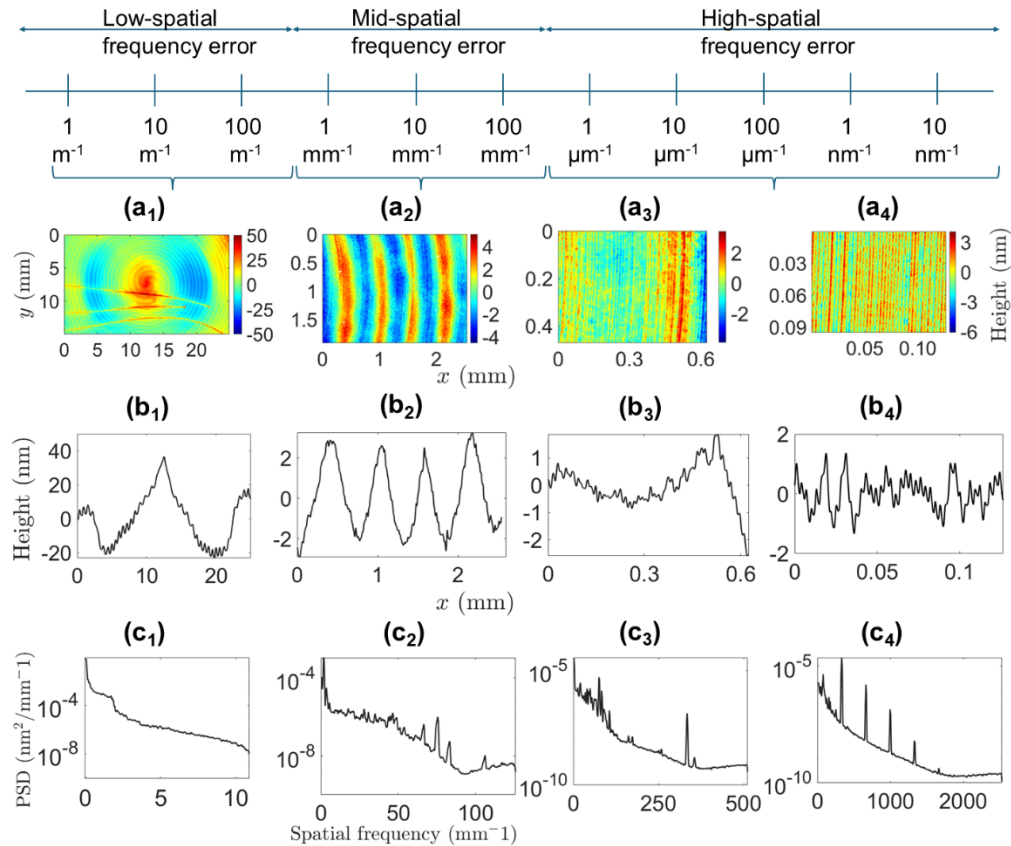


Fig. 3. Overview of spatial frequency-dependent features measured with various optical metrology systems. (a₁) Surface metrology measured by HDX and (a₂-a₄) measured by GT-X with objectives 2.5×, 10×, and 50×. (b₁-b₄) 1D height error of the surface (a₁-a₄) along the central tangential line with 1 mm slice. (c₁-c₄) Power spectral density profile of the surface maps (a₁-a₄).

Second, the beam removal function (BRF) of the ion beam for a chosen material is determined with high precision to correct the optic's form irregularity. We created several BRF craters on one of the NiP-coated samples and identified the BRF parameters, such as material etching rate and beam width.

Third, the dwell time map for the optical surface based on the BRF parameters is calculated using an algorithm, as shown in Fig. 4. In this work, we utilised a MATLAB-based code using the robust iterative Fourier transform dwell time algorithm (RIFTA), originally developed by Wang *et al.* [42] at the National Synchrotron Light Source II (NSLS-II) in Brookhaven National Laboratory, Upton, NY. The algorithm automatically calculates the required dwell time to correct an input surface using predefined BRF parameters and provides a residual surface map and material removal map. During the correction over the CA, half of the polishing tool (ion beam) falls outside the CA at the edge, producing edge effects as shown in Fig. 4(b₄). Therefore, correction is performed over an extended area known as the dwell grid (DG), which surrounds the CA with a width equal to the radius of the polishing tool. Various types of surface extension algorithms are applied to generate height in the DG by extrapolating the height within the CA to minimise edge effects and total dwell time, see Fig. 4(c₄). The bottom row of Figs. 4(c₁-c₄) show RIFTA simulation results with an eight-nearest-neighbours (8NN) surface extension as an

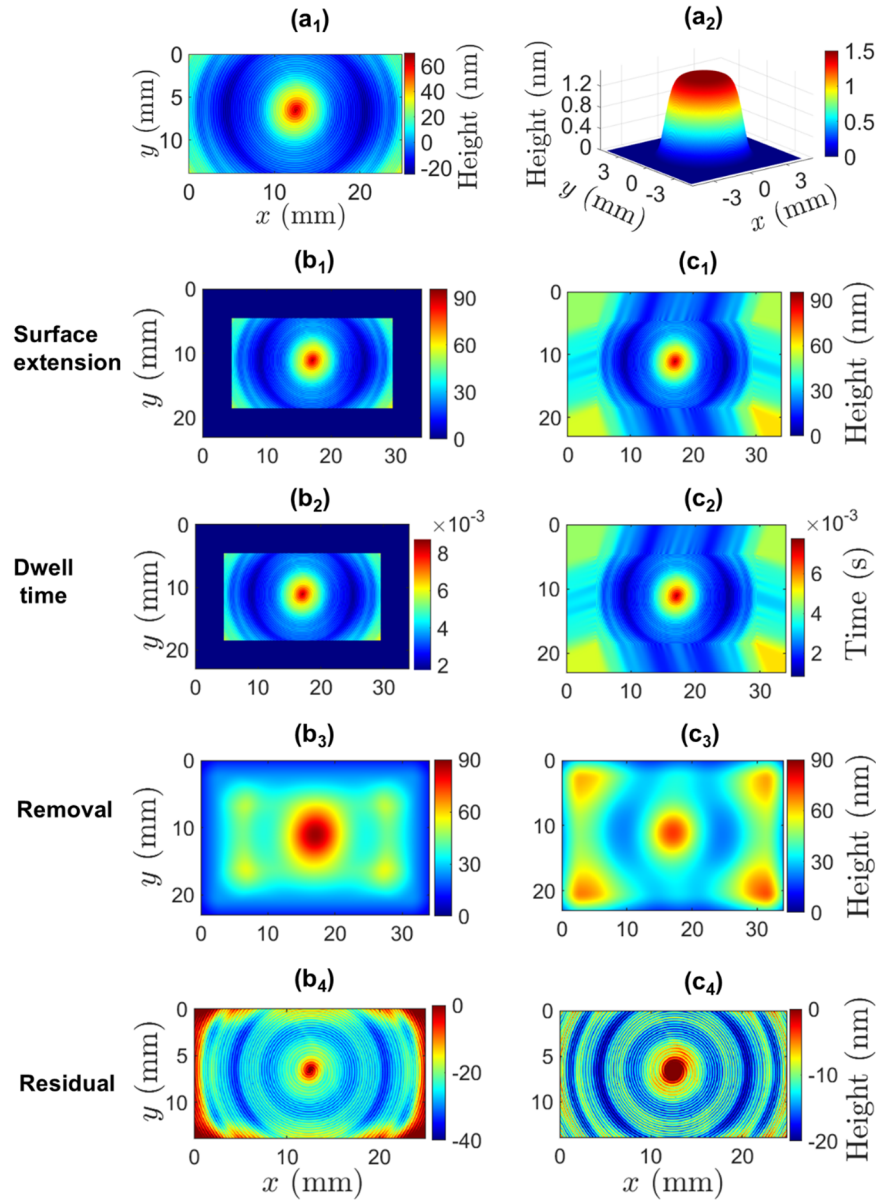


Fig. 4. RIFTA simulation results with and without surface extension. Top row, left to right (a₁-a₂): original surface within the clear aperture (CA), and optimized Gaussian BRF profile. Second column and last four rows, top to bottom (b₁-b₄): extended surface without any surface extrapolation, dwell time map, material removal map over the dwell grid, and residual surface map over CA. Third column and last four rows, top to bottom (c₁-c₄): same as for (b₁-b₄) but calculated for 8-nearest-neighbor surface extension.

example. During dwell time calculation, we consider multiple surface extensions and select the best one for the correction based on the mirror's residual surface quality.

Fourth, the extra material from the surface is removed by executing the calculated dwell time map of the ion beam over the optical surface. In our IBF system, the ion beam remains stationary, and the optic under correction is translated in front of the beam via a four-axis motion stage.

Finally, the surface is re-measured and compared to the results before correction. In some cases, multiple iterations are necessary to achieve the desired values for the optics.

It is important to note that the deterministic IBF process can only correct some specific spatial frequency features, depending on the size of the polishing tool (i.e., the ion beam). Spatial features smaller than the beam size, for instance, cannot be corrected by IBF.

4. Results and discussion

The results and discussion section are divided into three parts. In Section 4.1, the surface form error (SFE) correction results obtained on a flat surface using IBF is discussed. Then, SFE results obtained on a spherical surface are discussed in Section 4.2. Finally, Section 4.3 covers the SFE correction after removal of diamond turning marks.

4.1. Surface form error correction of a flat mirror

A NiP-coated mirror with a flat surface has been manufactured, and the SFE has been minimised using IBF. The surface morphology was measured before and after IBF using HDX stitching interferometry. After removing the best-fit cylinder (2nd order polynomial) from the surface, the height error before IBF was found to be 92.7 nm peak-to-valley (PV) and 16.3 nm RMS over the CA of 25 mm × 15 mm, as shown in Fig. 5(a). Figure 5(b) presents the SFE map of the mirror after IBF, again with the best-fit cylinder removed. Initially, a 5 mm diameter aperture was used to make a super-Gaussian ion beam (higher-order value, $P = 3.76$) with a full width at half maximum (FWHM) of approximately 4.4 mm and material etching rate of 1.48 nm/s

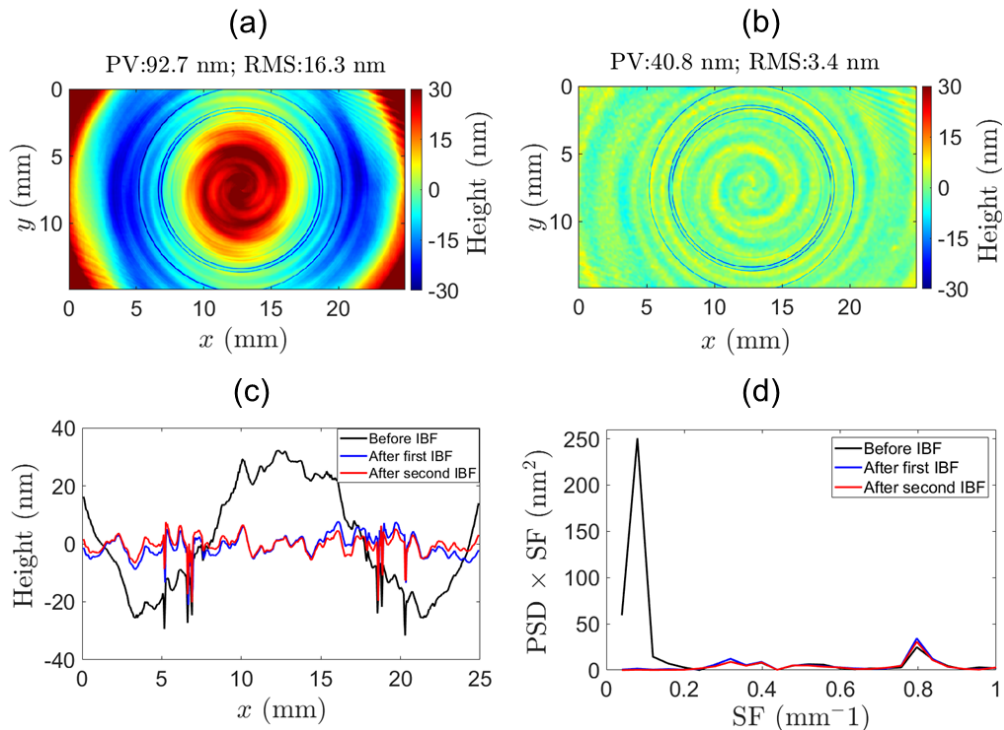


Fig. 5. Results of NiP flat mirror before and after IBF process. (a) Surface height error map before IBF; (b) surface height error after two iterations of IBF; (c) 1D height errors along a central tangential line before and after IBF; and (d) the product of power spectral density (PSD) and spatial frequency (SF) as a function of SF before and after IBF.

for coarse correction of the SFE. Subsequently, fine form error correction was achieved using a 3 mm aperture to generate a smaller ion beam ($P = 2.03$, $\text{FWHM} = 2.5$ mm, material etching rate = 1.45 nm/s). Notably, the material etching rate for NiP (1.45 nm/s) is slightly higher than that of single-crystalline silicon (Si) material (1.02 nm/s).

After two iterations of IBF, the height errors improved to 40.8 nm PV and 3.4 nm RMS as shown in Fig. 5(b). Figure 5(c) illustrates the height error along the length of the sample, averaged over a 1 mm-wide slice: before IBF (black line), after the first iteration of IBF (blue line), and after the second iteration (red line) of IBF. Figure 5(d) shows the the product of power spectral density (PSD) and spatial frequency (SF) with respect to the SF of the surface before IBF (black), after the first iteration of IBF (blue), and after the second iteration of IBF (red). The PSD data are calculated using the 1D height data as shown in Fig. 5(c), and plotted up to $\text{SF} = 1$. The features with spatial frequency below 0.2 mm^{-1} (corresponding to a spatial period of 5 mm) have been successfully removed, while the features with a higher SF (smaller spatial period) remain unchanged. This demonstrates that the MSF and HSF height errors of the mirror could not be corrected using IBF, due to limitations related to the tool size.

4.2. Surface form error correction of a spherical mirror

A NiP-coated spherical mirror with radius of curvature (ROC) of approximately 230 m has been machined by SPDT. The initial surface morphology measured by stitching interferometry is shown in Fig. 6(a). The surface map after subtraction of the target spherical component (ROC = 234 m) is shown in Fig. 6(b). It reveals a high height errors of 95.8 nm PV and 13.8 nm RMS over the CA of 25 mm \times 15 mm. For the coarse correction using IBF, a 5 mm aperture was used, as described in Section 4.1. For subsequent fine correction, a 1 mm aperture was used to create a smaller Gaussian beam ($\text{FWHM} = 0.98$ mm, material etching rate = 0.84 nm/s). The mirror surface height error map after IBF is shown in Fig. 6(c), which clearly demonstrates a significant improvement of the mirror surface. The form irregularity has been reduced to 63.8 nm PV and 4.4 nm RMS. Figure 6(d) shows the 1D tangential height error taken across the mirror before (black) IBF, after the first iteration (blue) of IBF, and after the second iteration (red) of IBF. These plots show the significant improvement in the height error after IBF, particularly for the LSF errors. Figure 6(e) shows the product of PSD and SF as a function of SF of the 1D height errors, demonstrating that only features with spatial frequency under 0.2 mm^{-1} have been corrected by IBF, similar to the results obtained for the flat surface described in Section 4.1. Figure 6(f) displays the measured shape of the mirror along the central tangential line before (black) IBF and after (red) IBF, with the nominal spherical shape shown in blue. The measured ROC of the mirror has improved from 280 m (before IBF, black line) to 232 m (after IBF, red line) which closely matches the target ROC of 234 m (blue line). IBF was highly successful at reducing the SFE for these mirrors; however, as in the case of these mirrors, the correction is limited by the presence of diamond turning marks, which cannot be effectively corrected using IBF.

4.3. Surface form error correction after removing the diamond turning marks

As discussed in Sections 4.1 and 4.2, improvement of the form errors of SPDT-produced surfaces using IBF is limited by the diamond turning marks. To further improve the surface, it is essential to remove the diamond turning marks prior to IBF, by using semi-stochastic polishing methods such as CMP.

To investigate this, a third NiP-coated mirror was prepared using SPDT, with a flat surface geometry. Figure 7(a) shows the SFE map of the mirror over a CA of 20 mm \times 10 mm, with circular diamond turning marks clearly visible. Two diagonal scratches are also present on the surface of the mirror. The NiP mirror was then polished using CMP, and the resulting SFE map is shown in Fig. 7(b). Following CMP, the diamond turning marks have been successfully removed;

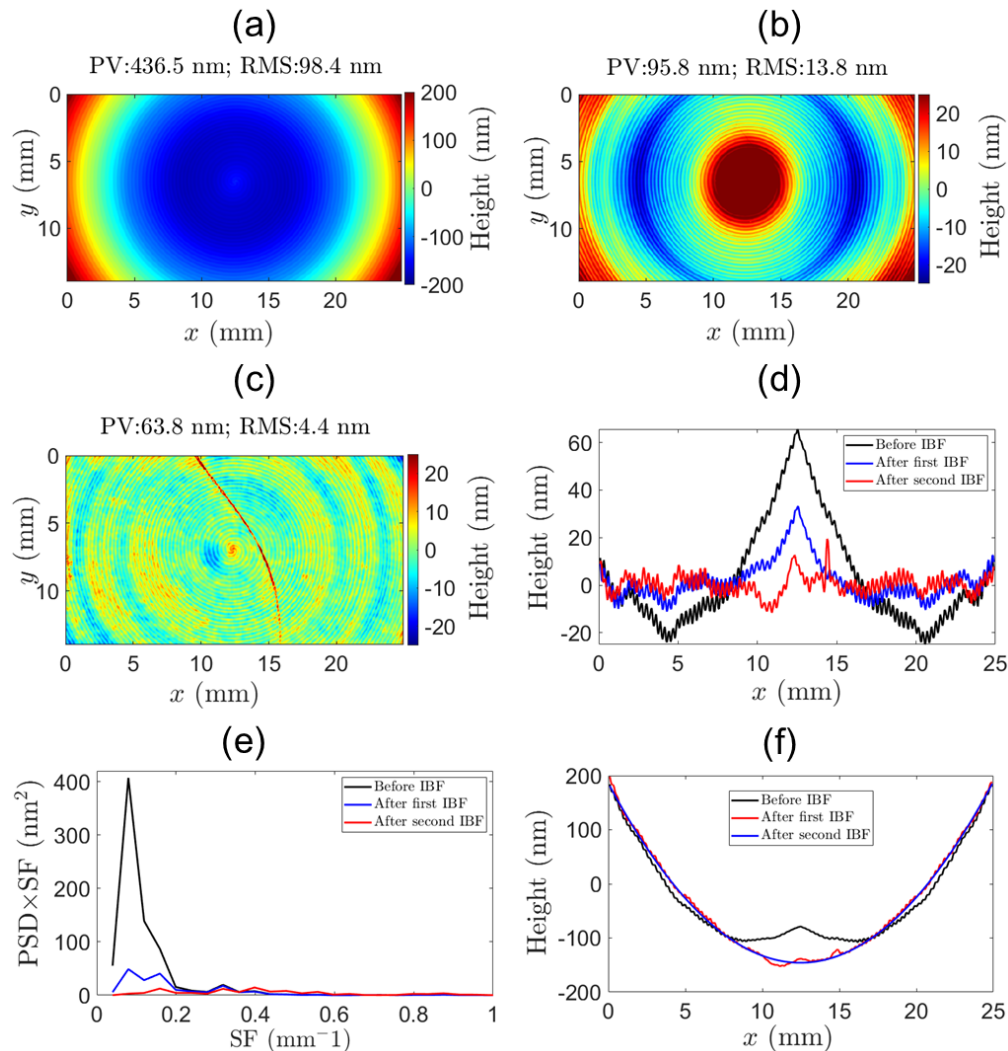


Fig. 6. Surface height error results of a NiP-coated spherical mirror before and after IBF corrections. (a) The surface height error map of the mirror as measured after SPDT, (b) the initial surface map following the removal of the spherical component over a CA of 25mm×15mm, which exhibits low-, mid-, and high-spatial frequency-dependent height errors, (c) the surface map over the CA after IBF, (d) 1D height errors along the central tangential line before and after IBF corrections, (e) the product of PSD and SF as a function of SF before and after IBF, and (f) the measured surface shape along the central tangential line compared to the ideal spherical profile before and after IBF corrections.

however, a significant LSF errors have been introduced to the optical surface, due to nature of the CMP polishing process. IBF was then used to correct these LSF errors. Figure 7(c) shows the SFE map of the mirror after IBF. The SFE has been reduced from 331.1 nm PV and 46.7 nm RMS to 78.1 nm PV and 4.1 nm RMS after IBF, representing more than an 11-fold improvement in the RMS error. This demonstrates the excellent efficiency of IBF in correcting LSF errors. When a low-pass slope filter is applied to remove the two scratches (which could not be corrected either by CMP or IBF), the RMS height error over the CA was further reduced from 4.1 nm to 1.9 nm RMS, as shown in Fig. 7(d).

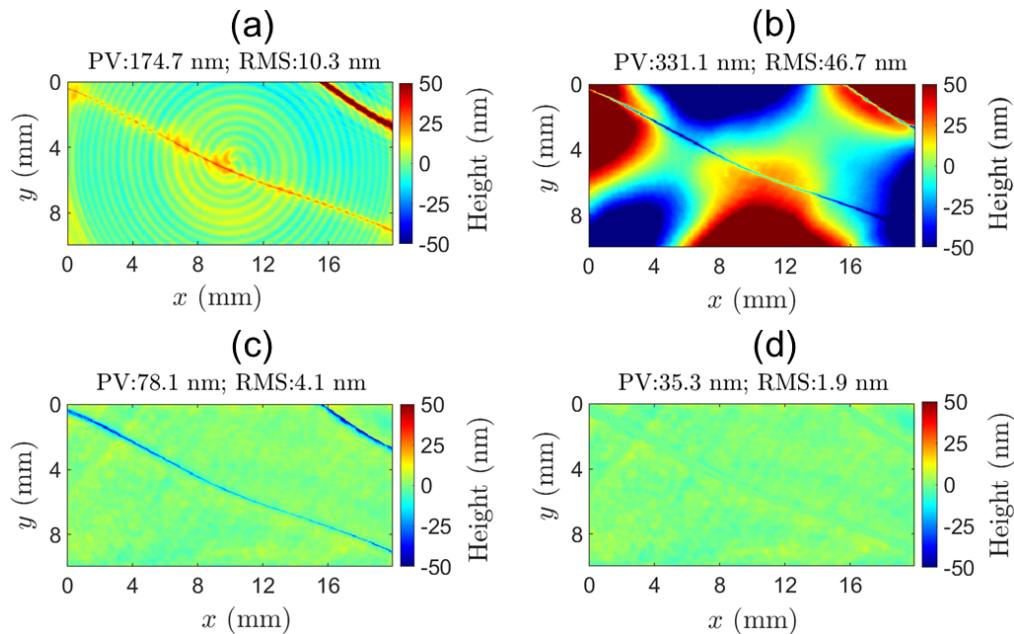


Fig. 7. Surface height error results of a NiP mirror after SPDT, CMP, and IBF. (a) Measured surface height error map of the mirror after SPDT, (b) surface map after CMP, which introduces low-spatial frequency height errors, (c) measured surface map over the CA after IBF, and (d) further processed data of (c) with a slope filter applied to remove the scratch lines.

4.4. Effect of IBF process on MSF and HSF surface roughness

For any surface-finishing technique, it is crucial to improve the surface quality within a targeted spatial frequency range without degrading other frequency ranges. To verify this, the MSF and HSF surface roughness of a NiP mirror were measured using a GT-X instrument with 2.5 \times , 10 \times , and 50 \times objectives, before and after IBF. The GT-X measurements were conducted with a vertical resolution of < 0.05 nm RMS over a range of 3 mm to 130 μ m and an in-plane resolution of 10 μ m to 0.1 μ m. Figure 8 presents the GT-X measurement results for the mirror, comparing the surface roughness maps before and after IBF. The top and bottom rows show the maps for each objective: 2.5 \times (a₁ and b₁), 10 \times (a₂ and b₂), and 50 \times (a₃ and b₃), respectively. The results indicate that MSF and HSF surface irregularities remain nearly unchanged after IBF, confirming that the IBF process does not compromise mid- and high-spatial frequency roughness while significantly reducing the LSF errors of the surface.

5. Conclusions

With the increasing use of metal optics for UV to IR telescopes, NiP-coated mirrors have significant development potential due to their excellent processing and optical properties. In this study, mirrors made of an AlSi40 substrate material were manufactured and then coated with NiP using electroless nickel plating. The optical surfaces were subsequently machined using SPDT, and the residual SFE was corrected using IBF. A variety of surface types were tested for IBF correction. The flat mirror SFE was improved from 16.3 nm to 3.4 nm RMS, while the spherical mirror SFE was reduced from 13.8 nm to 4.4 nm RMS, with the mirror shape becoming much closer to the target spherical form. In both cases, the SFE correction was limited by diamond turning marks. To remove these turning marks, a flat NiP mirror was polished using CMP after

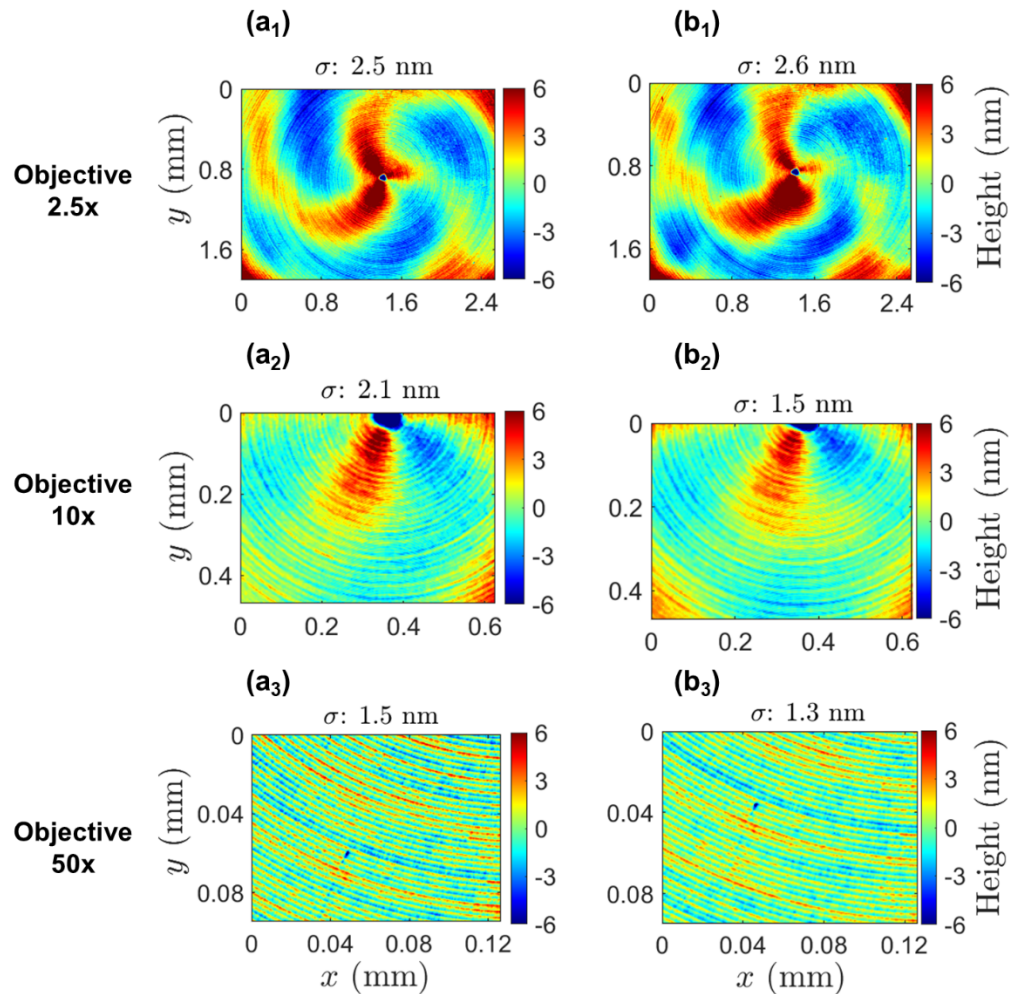


Fig. 8. GT-X measurements of a NiP-mirror before and after IBF. (a₁-a₃) Surface roughness maps measured with 2.5×, 10×, and 50× objectives before IBF; (b₁-b₃) corresponding surface roughness maps measured after IBF. Here, σ corresponds to the RMS surface roughness.

SPDT. IBF was then used on the polished mirror to reduce the height error and then refined using IBF, demonstrating that the surface height error is further reduced to 1.9 nm RMS. It was also verified that IBF does not degrade surface waviness and micro roughness. These results show that IBF is a suitable technique for figuring NiP-coated mirrors and can be used to efficiently achieve, surface height errors below 2 nm RMS.

Funding. This research was funded by the UK Space Agency Enabling Technology Program round 1 Grant reference number (ETP01-040). This project has received funding from the European Union's Horizon 2020 Framework Programme under grant agreement number.(101004728).

Acknowledgments. The IBF work was carried out with the support of Diamond Light Source Ltd, UK. The authors would like to thank Andrew Malandain, Adam Howell, Nicholas Rubies, and the staff at Diamond for their invaluable technical assistance in maintaining, using, and upgrading of the IBF system. Also, the authors are grateful to Murilo Bazan Da Silva, Ioana-Theodora Nistea, and Simon Alcock for assistance with measurements and valuable discussions on metrology data analysis. For their expertise in diamond machining, the authors would like to thank Paul White and Ken Parkin for their contributions to the SPDT work in Durham.

Disclosures. The authors declare that there are no conflicts of interest related to this article.

Data availability. Data underlying the results presented in this paper are not publicly available at this time but may be obtained from the authors upon reasonable request.

References

1. C. Graham, J. M. Girkin, and C. Bourgenot, "Freeform based hYperspectral imager for MOisture Sensing (FYMOS)," *Opt. Express* **29**(11), 16007 (2021).
2. P. Van Doorn, D. Nijkerk, B. van Venrooy, *et al.*, "The TROPOMI Telescope," in (*SPIE-Intl Soc Optical Eng*), p. 21 (2017).
3. A. Reutlinger, S. Eberle, C. Wilsnack, *et al.*, "Printed Athermal Mirror (PAM) based on AlSi40 and NiP coating for space application," in (*SPIE-Intl Soc Optical Eng*, 2023), p. 105.
4. S. Risse, A. Gebhardt, C. Damm, *et al.*, "Novel TMA telescope based on ultra precise metal mirrors," in *Space Telescopes and Instrumentation 2008: Optical, Infrared, and Millimeter (SPIE)*, 7010, p. 701016 (2008).
5. E. Hilpert, J. Hartung, H. von Lukowicz, *et al.*, "Design, additive manufacturing, processing, and characterization of metal mirror made of aluminum silicon alloy for space applications," *Opt. Eng.* **58**(09), 1 (2019).
6. W. P. Barnes, *Basic Properties of Metal Optics* (n.d.).
7. S. Scheiding, C. Damm, W. Holota, *et al.*, "Ultra-precisely manufactured mirror assemblies with well-defined reference structures," in *Modern Technologies in Space- and Ground-Based Telescopes and Instrumentation (SPIE)*, 7739, p. 773908 (2010).
8. R.-R. Rohloff, A. Gebhardt, V. Schönherr, *et al.*, "A novel athermal approach for high-performance cryogenic metal optics," in *Modern Technologies in Space- and Ground-Based Telescopes and Instrumentation (SPIE)*, 7739, p. 77394E (2010).
9. M. Beier, J. Hartung, T. Peschel, *et al.*, "Development, fabrication, and testing of an anamorphic imaging snap-together freeform telescope," *Appl. Opt.* **54**(12), 3530 (2015).
10. Y. Xie, X. Mao, J. Li, *et al.*, "Optical design and fabrication of an all-aluminum unobscured two-mirror freeform imaging telescope," *Appl. Opt.* **59**(3), 833 (2020).
11. Z. Shen, J. Yu, Z. Song, *et al.*, "Customized design and efficient fabrication of two freeform aluminum mirrors by single point diamond turning technique," *Appl. Opt.* **58**(9), 2269 (2019).
12. C. Atkins, W. Brzozowski, N. Dobson, *et al.*, "Additively manufactured mirrors for CubeSats," in *Astronomical Optics: Design, Manufacture, and Test of Space and Ground Systems II*, T. B. Hull, D. W. Kim, and P. Hallibert, eds. (SPIE), 11116, pp. 335–352 (2019).
13. C. Atkins, Y. Cahid, G. Lister, *et al.*, "Targeting low micro-roughness for 3D printed aluminium mirrors using a hot isostatic press," in (*SPIE-Intl Soc Optical Eng*), p. 141 (2024).
14. J. Wang, X. Bai, X. Shen, *et al.*, "Effect of micro-texture on substrate surface on adhesion performance of electroless Ni–P coating," *J. Manuf. Process.* **74**, 296–307 (2022).
15. J. Kinast, M. Beier, A. Gebhardt, *et al.*, "Polishability of thin electrolytic and electroless NiP layers," in *Optifab (SPIE)*, 2015, 9633, p. 963311 (2015).
16. L. Li, X. Min, D. Chen, *et al.*, "Special techniques in ultra-precision machining," in *3rd International Symposium on Advanced Optical Manufacturing and Testing Technologies: Advanced Optical Manufacturing Technologies (SPIE)*, 6722, p. 672213 (2007).
17. Y. Namba, T. Shimomura, A. Fushiki, *et al.*, "Ultra-precision polishing of electroless nickel molding dies for shorter wavelength applications," *CIRP Ann.* **57**(1), 337–340 (2008).
18. O. W. Fä Hnle, H. Van Brug, and H. J. Frankena, *Fluid Jet Polishing of Optical Surfaces* (1998).
19. A. Beaucamp and Y. Namba, "Super-smooth finishing of diamond turned hard X-ray molding dies by combined fluid jet and bonnet polishing," *CIRP Ann.* **62**(1), 315–318 (2013).
20. Z. Yin and Z. Yi, "Direct polishing of aluminum mirrors with higher quality and accuracy," *Appl. Opt.* **54**(26), 7835 (2015).
21. C. Xu, X. Peng, J. Liu, *et al.*, "A High Efficiency and Precision Smoothing Polishing Method for NiP Coating of Metal Mirror," *Micromachines (Basel)* **13**(8), 1171 (2022).
22. K. Qin, B. Moudgil, and C. W. Park, "A chemical mechanical polishing model incorporating both the chemical and mechanical effects," *Thin Solid Films* **446**(2), 277–286 (2004).
23. X. Chen, Y. Zhao, Y. Wang, *et al.*, "Nanoscale friction and wear properties of silicon wafer under different lubrication conditions," *Appl. Surf. Sci.* **282**, 25–31 (2013).
24. R. Shurvinton, H. Wang, P. Pradhan, *et al.*, "Ion beam figuring for X-ray mirrors: history, state-of-the-art and future prospects," *J. Synchrotron Radiat.* **31**(4), 655–669 (2024).
25. J. Liu, X. Li, Y. Zhang, *et al.*, "Predicting the Material Removal Rate (MRR) in surface Magnetorheological Finishing (MRF) based on the synergistic effect of pressure and shear stress," *Appl. Surf. Sci.* **504**, 144492 (2020).
26. Z. Lin, H. Hu, Y. Dai, *et al.*, "Prediction of surface roughness and the material removal rate in magnetorheological finishing," *Opt. Express* **30**(26), 46157 (2022).
27. C. Xu, X. Peng, J. Liu, *et al.*, "Nano-Precision processing of NiP coating by magnetorheological finishing," *Nanomaterials* **13**(14), 2118 (2023).
28. M. Ulitschka, J. Bauer, F. Frost, *et al.*, "Improvement of the optical properties after surface error correction of aluminium mirror surfaces," *J. Eur. Opt. Soc.-Rapid Publ.* **17**(1), 1 (2021).

29. J. Bauer, "Finishing of metal optics by ion beam technologies," *Opt. Eng.* **58**(09), 1 (2019).
30. Y. Li, H. Takino, and F. Frost, "Ion beam planarization of diamond turned surfaces with various roughness profiles," *Opt. Express* **25**(7), 7828 (2017).
31. T. Wang, L. Huang, Y. Zhu, *et al.*, "Ion Beam Figuring System for Synchrotron X-Ray Mirrors Achieving Sub-0.2- μ rad and Sub-0.5-nm Root Mean Square," *Nanomanuf. Metrol.* **6**(1), 20 (2023).
32. H. Thiess, H. Lasser, and F. Siewert, "Fabrication of X-ray mirrors for synchrotron applications," *Nucl. Instrum. Methods Phys. Res., Sect. A* **616**(2-3), 157–161 (2010).
33. A. Majhi, R. Shurvinton, P. C. Pradhan, *et al.*, "Sub-nanometre quality X-ray mirrors created using ion beam figuring," *J. Synchrotron Radiat.* **31**(4), 706–715 (2024).
34. M. Weiser, "Ion beam figuring for lithography optics," *Nucl. Instrum. Methods Phys. Res., Sect. B* **267**(8-9), 1390–1393 (2009).
35. M. Zeuner and S. Kiontke, "Ion Beam Figuring Technology in Optics Manufacturing," *Opt. Photonik* **7**(2), 56–58 (2012).
36. R. Steinkopf, A. Gebhardt, S. Scheiding, *et al.*, "Metal mirrors with excellent figure and roughness," *Proc. of SPIE*, 7102 7102C (2008).
37. S. Scheiding, C. Damm, W. Holota, *et al.*, "Ultra precisely manufactured mirror assemblies with well defined reference structures," *Proc. of SPIE*, 7739 773908 (2010).
38. C. Bourgenot, V. Krumins, D. G. Bramall, *et al.*, "Topology Optimization of a Single-Point Diamond-Turning Fixture for a Deployable Primary Mirror Telescope," *Aerospace* **11**(1), 50 (2024).
39. M. B. Da Silva, S. G. Alcock, I.-T. Nistea, *et al.*, "A fizeua interferometry stitching system to characterize X-ray mirrors with sub-nanometre errors," *Optics and Lasers in Engineering* **161**, 107192 (2023).
40. S. G. Alcock, I. Nistea, and K. Sawhney, "Nano-metrology: The art of measuring X-ray mirrors with slope errors <100 nrad," *Rev. Sci. Instrum.* **87**(5), 051902 (2016).
41. M. Hand, S. G. Alcock, M. Hillman, *et al.*, "Ion beam figuring and optical metrology system for synchrotron x-ray mirrors," in (*SPIE-Intl Soc Optical Eng*), p. 9 (2019).
42. T. Wang, L. Huang, H. Kang, *et al.*, "RIFTA: A Robust Iterative Fourier Transform-based dwell time Algorithm for ultra-precision ion beam figuring of synchrotron mirrors," *Sci. Rep.* **10**(1), 8135 (2020).